# Supporting Information for "Influence of Shear Heating and Thermomechanical Coupling on Earthquake Sequences and the Brittle-Ductile Transition"

Kali L. Allison[1,2], Eric M. Dunham[1,3]

[1]Department of Geophysics, Stanford University, Stanford, California, USA

[2]now at: Department of Geology, University of Maryland, College Park, Maryland, USA

[3]Institute for Computational and Mathematical Engineering, Stanford University, Stanford, California, USA

## 1. Numerical Method

The discretization of the governing equations is a straightforward extension of previous work. We employ the Cartesian grid finite difference method developed by Erickson & Dunham (2014) and Allison & Dunham (2018) to solve the static elasticity and heat equations, both on the same grid. We select the along-fault grid spacing to resolve the nucleation length (e.g., Ruina, 1983; Rice, 1983, 1993; Rice et al., 2001),

$$h^* = \frac{\mu d_c}{\sigma_n (b-a)} \tag{1}$$

and the cohesive-zone size (Dieterich, 1992; Ampuero & Rubin, 2008),

$$L_b = \frac{\mu d_c}{\sigma_n b}, \tag{2}$$

which is generally smaller than $h^*$. In the fault-normal direction, we must resolve thermal boundary layers near the fault, the width of which will be no larger than $w$. Therefore, we use a grid spacing of $L_b/4$ in the $z$-direction in the seismogenic zone, and $w/5$ in the $y$-direction near the fault, with aggressive grid stretching outside of this region.

We next explain time stepping. We utilize the explicit Runge–Kutta algorithm with adaptive time-step selection described in Allison & Dunham (2018) to update slip, state variable, and viscous strains. However, stiffness of the heat equation requires implicit time-stepping for efficiency. To handle this, we use operator splitting, updating temperature in the heat equation with backward Euler after each full adaptive step.

Specifically, during each adaptive Runge–Kutta time step from time $t^n$ to $t^{n+1} = t^n + \Delta t$, temperature is held fixed at $\Delta T^n$ while solving for slip $\delta^{n+1}$, state $\psi^{n+1}$, and the viscous strains $\gamma_{xy}^{n+1}$ and $\gamma_{xz}^{n+1}$. We then compute the stresses at $t^{n+1}$, and the flow law provides the viscous strain rates $\dot{\gamma}_{xy}^{n+1}$ and $\dot{\gamma}_{xz}^{n+1}$. Then, these fields are held fixed and used to compute the shear heating source term $Q^{n+1}$ when solving for $\Delta T^{n+1}$.

## 2. Stresses

The similarities and differences between these three simulations featured in Figure 4 can also be seen in the temporal evolution of shear stress on the fault and its deep extension, plotted in Figure S1. In the upper crust, the shear stress is very similar in all three simulations, because the off-fault material is effectively elastic and stress is limited by the frictional strength of the fault. At greater depths, around 23 km in the viscoelastic simulation without shear heating and 15 km in the viscoelastic simulation with shear heating, the viscoelastic material becomes much weaker than the frictional strength of the fault, resulting in a much weaker shear stress than in the elastic simulation.

## 3. Influence of Pore Pressure on Contributions to Shear Heating

Figure S2 explores the influence of pore pressure, parametrized through $\lambda$, on the thermal anomaly.

## 4. Thermal Energy

One way of summarizing the results of our parameter space search is to integrate the thermal anomaly times the heat capacity over the domain, producing the thermal energy per unit length $\theta$. As shown in Figure S3, the total thermal energy increases with deeper LAB depths. It also decreases slightly with increasing pore pressure, but this is a much smaller effect. Also, for all the parameters considered, both frictional and viscous shear heating contribute substantially to the total thermal energy in the system, with viscous shear heating constituting more than half the total (except for the simulation with a 70 km deep LAB and $\lambda = 0.8$).

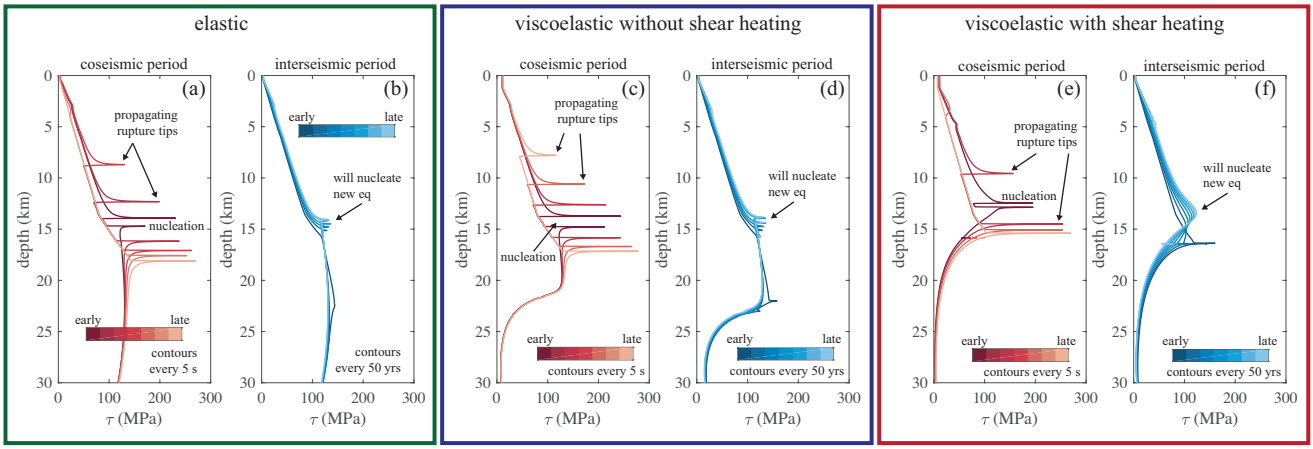


**Figure S1.** Comparison of the temporal evolution of shear stress on the fault and its deep extension in elastic, viscoelastic without shear heating, and viscoelastic with shear heating cycle simulations, for an LAB of 50 km and hydrostatic pore pressure. (a), (c) and (e) First 20 s of the coseismic period, with contours plotted every 5 s. (b), (d) and (f) Interseismic period with contours plotted every 50 years.

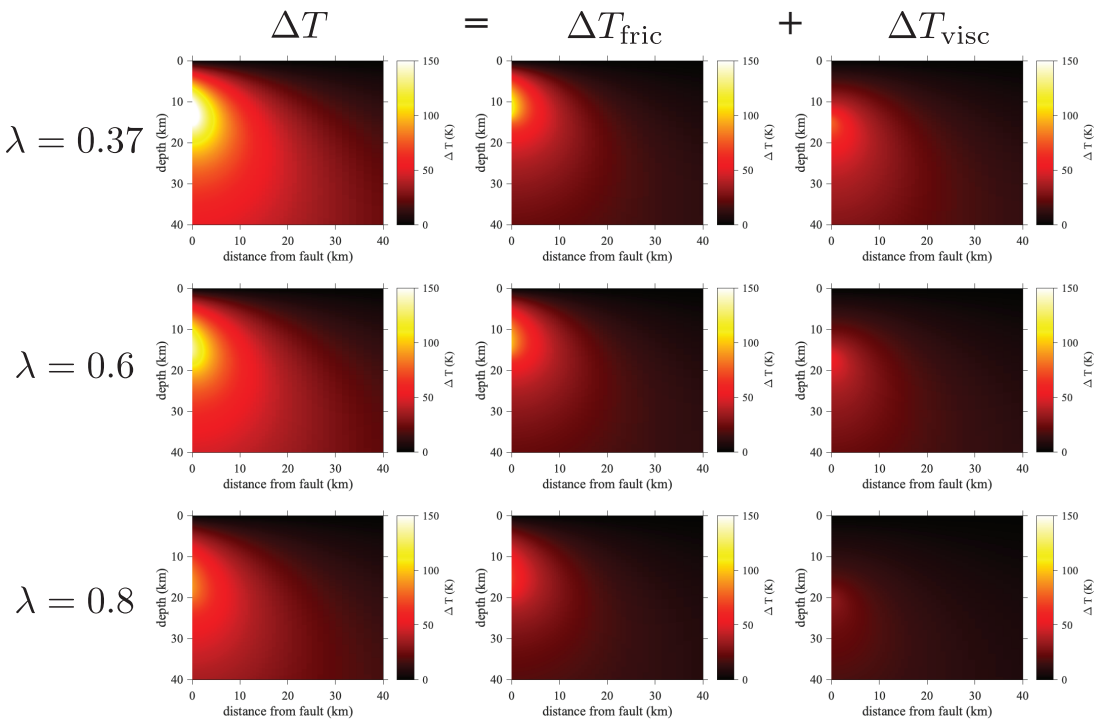


**Figure S2.** Comparison of $\Delta T$ and its components $\Delta T_{\text{fric}}$ and $\Delta T_{\text{visc}}$, as a function of $\lambda$, for a simulation with a 50 km deep LAB.

## 5. Temperatures of Various Transitions

The temperatures which correspond with the depths plotted in Figure 8 are shown in Figure S4.

## 6. Comparison of Steady-State and Cycle-Averaged Results

Figures S5 and S6 compare steady-state and cycle-averaged results.

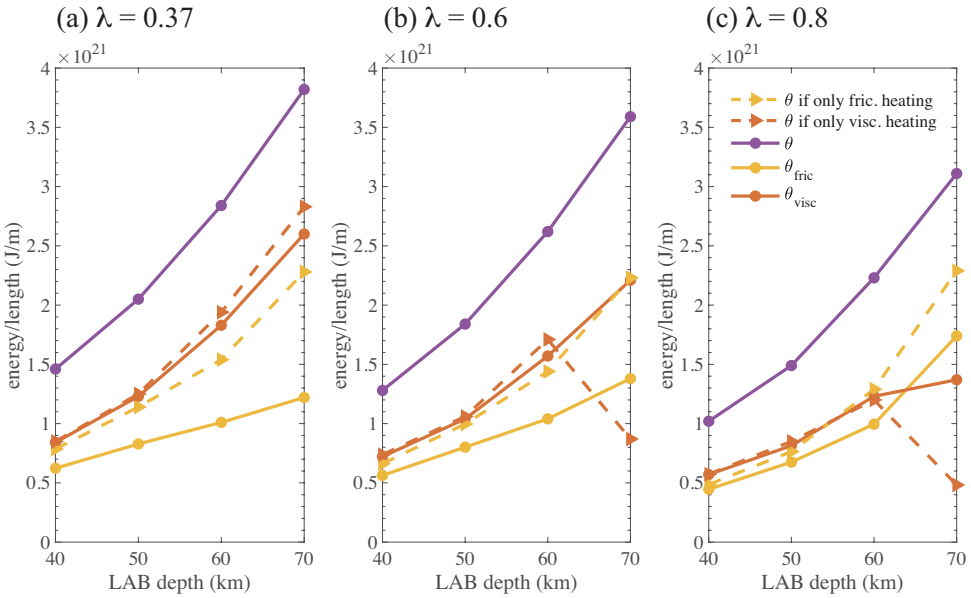


**Figure S3.** Total thermal energy $\theta$ (purple), portion of total thermal energy contributed by frictional $\theta_{\text{fric}}$ (yellow, solid lines) and viscous $\theta_{\text{visc}}$ (red, solid lines)) shear heating, total energy from simulations with only frictional shear heating (yellow, dashed lines), and total energy from simulations with only viscous shear heating (red, dashed lines), as a function of LAB depth and pore pressure.

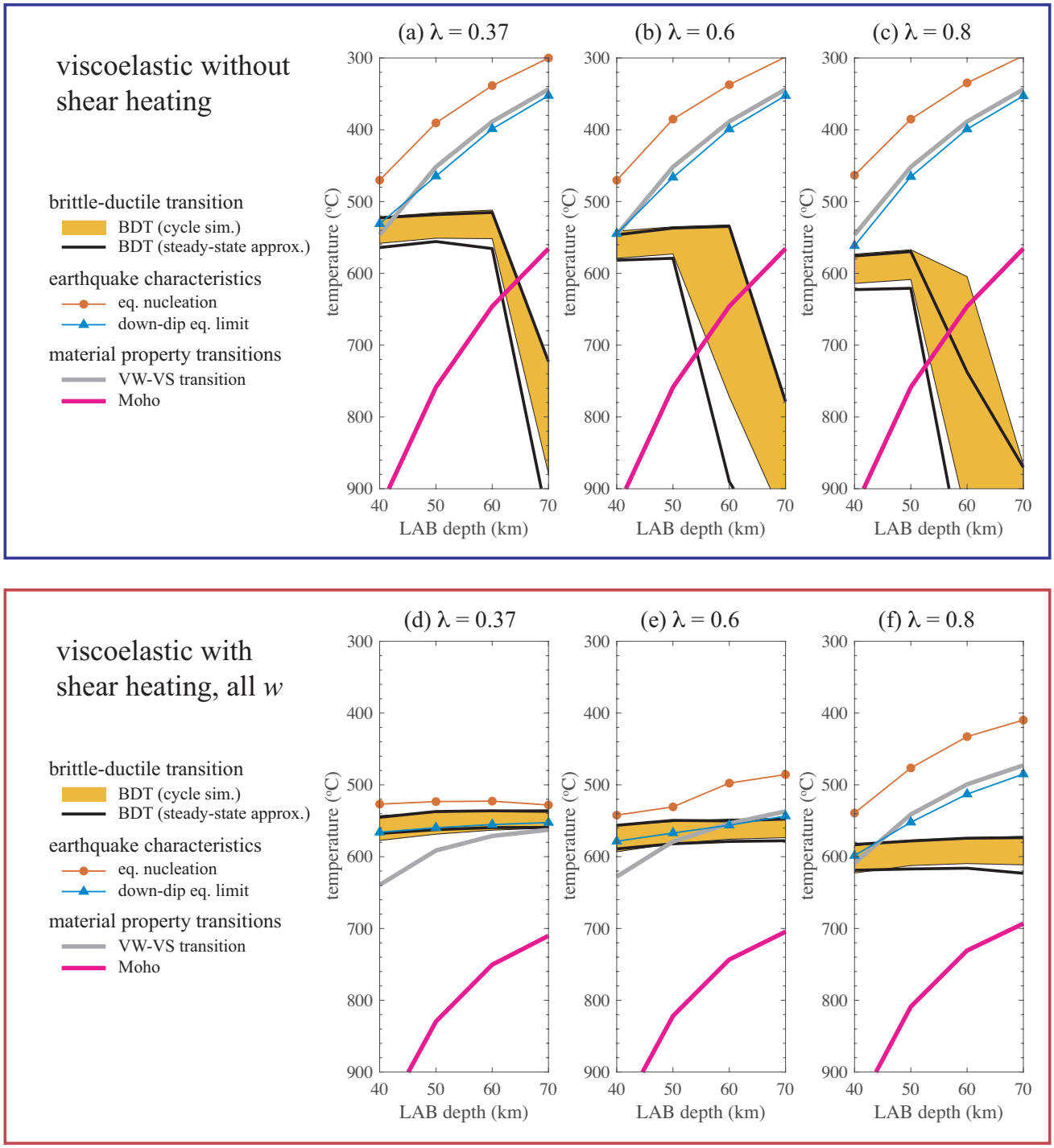


**Figure S4.** Comparison between the temperatures of earthquake nucleation (red circles), the down-dip limit of coseismic slip (blue triangles), and the BDT temperature range (yellow filled regions) for simulations with and without shear heating. For the viscoelastic simulations with shear heating, the average interseismic temperature is used. Also shown are estimates of the BDT temperatures from steady-state results (black lines).

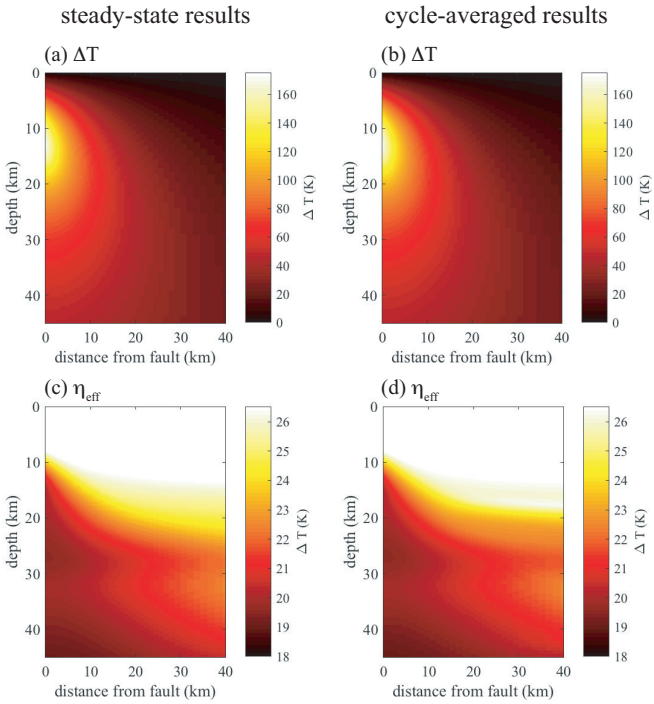


**Figure S5.** Comparison between steady-state and cycle-averaged results: thermal anomaly (a and b), and effective viscosity (c and d). Results are for a 50 km deep LAB and hydrostatic pore pressure.

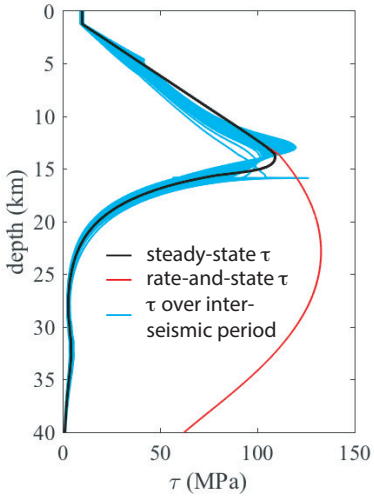


**Figure S6.** The steady-state shear stress on the fault and its deep extension (black) shows good agreement with the interseismic shear stress (blue) for a viscoelastic cycle simulation with shear heating, with a 50 km deep LAB and $\lambda = 0.37$. Also shown, for reference, is the shear stress for rate-and-state friction assuming the fault is sliding at the tectonic loading velocity (red).

## References


Allison, K. L., & Dunham, E. M. (2018). *Earthquake cycle simulations with rate-and-state friction and power-law viscoelasticity* (Vol. 733). doi: 10.1016/j.tecto.2017.10.021

Ampuero, J.-P., & Rubin, A. M. (2008). Earthquake nucleation on rate and state faults - Aging and slip laws. *Journal of Geophysical Research*, *113*(B1). Retrieved from http://doi.wiley.com/10.1029/2007JB005082 doi: 10.1029/2007JB005082

Dieterich, J. H. (1992). Earthquake nucleation on faults with rate-and state-dependent strength. *Tectonophysics*, *211*(1), 115–134. doi: 10.1016/0040-1951(92)90055-B

Erickson, B. A., & Dunham, E. M. (2014). An efficient numerical method for earthquake cycles in heterogeneous media: Alternating subbasin and surface-rupturing events on faults crossing a sedimentary basin. *Journal of Geophysical Research: Solid Earth*, *119*(4), 3290–3316. Retrieved from http://doi.wiley.com/10.1002/2013JB010614 doi: 10.1002/2013JB010614

Rice, J. R. (1983). Constitutive relations for fault slip and earthquake instabilities. *Pure and Applied Geophysics PAGEOPH*, *121*(3), 443–475. doi: 10.1007/BF02590151

Rice, J. R. (1993). Spatiotemporal complexity of slip on a fault. *Journal of Geophysical Research*, *98*(B6), 9885–9907. Retrieved from http://doi.wiley.com/10.1029/93JB00191 doi: 10.1029/93JB00191

Rice, J. R., Lapusta, N., & Ranjith, K. (2001). Rate and state dependent friction and the stability of sliding between elastically deformable solids. *Journal of the Mechanics and Physics of Solids*, *49*, 1865–1898. Retrieved from http://linkinghub.elsevier.com/retrieve/pii/S0022509601000424 doi: 10.1016/S0022-5096(01)00042-4

Ruina, A. (1983). Slip instability and state variable friction laws. *Journal of Geophysical Research: Solid Earth*, *88*(B12), 10359–10370. Retrieved from http://doi.wiley.com/10.1029/JB088iB12p10359 doi: 10.1029/JB088iB12p10359